Applied Physics B (2019) 125:223
https://doi.org/10.1007/s00340-019-7336-3

Applied Physics B
Lasers and Optics

Novel approach to passivation of InAs/GaSb type II superlattice photodetectors

E. Papis-Polakowska[1] · J. Kaniewski[1] · A. Jasik[1] · K. Czuba[1] · I. Sankowska[1] · P. Karbownik[2] · T. Runka[3] · T. Martyński[3] · J. Makowiecki[3] · A. Łapiński[4]

Received: 26 February 2019 / Accepted: 27 October 2019 / Published online: 5 November 2019
© The Author(s) 2019

Abstract

The innovative two-step passivation by octadecanethiol (ODT) self-assembled monolayers (SAMs) and the following silicon dioxide (SiO_2) deposition was used for the type-II InAs/GaSb superlattice photodetector. To understand the mechanism of passivation, the (100) GaSb surface covered with the ODT and, for comparison, with the biphenyl thiol (BPT), was characterized by the atomic force microscopy, Raman spectroscopy and contact angle analysis. The results of the study indicated the presence of the homogeneous both the ODT and the BPT monolayers; however, the ODT SAMs were more stable. Therefore, the ODT-based wet treatment was used in the two-step passivation resulting in a reduction of the dark current by one order of magnitude for passivated detector compared with an unpassivated device.

1 Introduction

The infrared (IR) detection has become an inevitable need for a wide range of applications in industry, medicine, space exploration as well as other important areas of technology and science. HgCdTe system, commonly used in IR photodetectors, has some limitations, especially for mid- and long-infrared wavelengths due to the low-binding energy of HgTe which can result in the evaporation of Hg or HgTe and, consequently, in degradation of the detector characteristics. Type-II InAs/GaSb superlattice (T2SL) is an alternative material for the next generation of IR detection systems for the wide flexibility in a cutoff wavelength design and the potential in quality and performance of devices [1, 2]. However, the GaSb-based surface is extremely reactive which can introduce additional surface states, causing the high surface recombination velocity and consequently, large leakage currents. To clarify, the dangling bonds on the GaSb-based surface can lead to an abrupt change of the device structure which results in the surface states within the forbidden band gap. During the exposure to the atmosphere, the dangling bonds initiate a chemical reaction with oxygen, causing the formation of the native oxides and a free Sb. To prevent this, it is necessary to use a special passivating layer which can protect the surface/interface prior to the oxidation (an encapsulate passivation) and remove the interfacial states from the band gap (electronic passivation). Therefore, the choice of a suitable passivant material and an applicable passivation technique is one of the important problems in the antimonide-based photodetector technology. A thick layer of dielectric (SiO_2, SiN_x) or organic material (polyimide, SU-8) can be used successfully for the encapsulation of detector sidewalls [3–5]. The application of chalcogenides or the overgrowth of a wide bandgap semiconductor layer represents the two main directions of approach to electronic passivation [6, 7]. According to our earlier studies, the $(NH_4)_2S$-based passivation is not suitable for the T2SL InAs/GaSb photodetector due to the mesa etching and leave sulfur residues [8]. It is very important to emphasize that no universal passivation method of the T2SL InAs/GaSb detector has been developed.

In the previous paper, the self-assembled monolayers (SAMs) of long-chain octadecanethiol (ODT) have been proposed as a new electronic passivant for T2SL InAs/GaSb

✉ E. Papis-Polakowska
papis@ite.waw.pl

[1] Łukasiewicz Research Network - Institute of Electron Technology, al. Lotników 32/46, 02-668 Warsaw, Poland

[2] Center of Development and Implementation, Telesystem-Mesko Sp. z o.o, ul. Warszawska 51, 05-082 Lubiczów, Poland

[3] Faculty of Technical Physics, Poznan University of Technology, ul. Piotrowo 3, 60-965 Poznan, Poland

[4] Institute of Molecular Physics, Polish Academy of Sciences, ul. M. Smoluchowskiego 17, 60-179 Poznan, Poland

detector [9]. SAMs have been found as the crucial electronically active inter-monolayers in GaAs and InP devices [10–12], whereas their application in GaSb-based systems is still open. It is known that is difficult to obtain the SAMs total coverage on the semiconductor surface [13, 14]. In particular, the uniformity of the SAMs layers is important in their application for T2SL InAs/GaSb detector passivation. Therefore, it is necessary to clarify the mechanism of interaction between SAMs and GaSb and InAs surface/interface. It is one of the main motivations for the research discussed in this paper.

On the other hand, the function of SAMs in devices depends both on the chemical structure of the molecules, and their final arrangement and orientation on the surface. For many applications, alkanethiols like octadecanethiol (ODT) are more appropriate. However, aromatic thiols like biphenyl thiol (BPT) offer a better-organized film structure compared to alkanethiol due to their greater rigidity and larger intermolecular interactions [15, 16].

In this paper, we presented a new two-step passivation method (ODT SAMs and SiO_2 deposition) for T2SL InAs/GaSb infrared detector. To understand the mechanism of passivation, the (100) GaSb surfaces covered with two different ODT and BPT SAMs were characterized in terms both of topography and chemical composition. The chemistry of (100) GaSb surafce was analyzed by Raman spectroscopy, while the surface morphology was examined by atomic force microscopy (AFM). The contact angle measurements have been used for characterization of the surface properties of SAMs in macroscopic scale. The electrical properties of detector were monitored using a current–voltage measurement.

2 Experimental

InAs/GaSb superlattice material was grown by molecular beam epitaxy (MBE) on nominally undoped (100) GaSb substrate. The detector structure consists of a 1400 nm Be-doped GaSb contact layer ($p = 1 \times 10^{18}$ cm^{-3}), a 130 nm p-doped GaSb layer ($Be = 1 \times 10^{17}$ cm^{-3}), 40 periods of a p-type doped InAs/GaSb:Be ($p = 1 \times 10^{17}$ cm^{-3}) superlattice, 400 periods of an undoped InAs/GaSb SL, 60 periods of n-type doped InAs:Te ($n = 5{\times}10^{17}$ cm^{-3})/GaSb SL and a 20 nm thick n-doped InAs cap layer ($n = 5{\times}10^{17}$ cm^{-3}). The layer thicknesses in each of the superlattices are as follows: 0.5 ML (0.14 nm) GaAs/9.2 ML InAs/1.5 ML (0.5 nm) InSb/10.5 ML GaSb. The high-resolution X-ray diffraction using the PANalytical X'Pert PRO Diffractometer was used to provide the information both on the quality and the thickness of layers in the GaSb/InAs periodical layered structures.

The mesa-type detector with an active area from 0.03 mm^2 to 0.14 mm^2 was performed employing standard optical lithography and dry BCl_3/Ar plasma etching. Then, an ohmic contact was defined by the evaporation of Ti (500 Å)/Pt (500 Å)/Au (3000 Å) on the top and the bottom contact layers of the detector structure. The scheme of T2SL InAs/GaSb detector after processing and the SEM image of the side wall of mesa structure are shown in Fig. 1 and 2, respectively. The current–voltage (I–V) characteristics in both forward and reverse-bias mode were measured at different temperatures in the range (75–300 K). The values of the leakage current density were used to determine passivation effectiveness. In addition, the spectral current responsivity measurements were performed for the sample photodetectors.

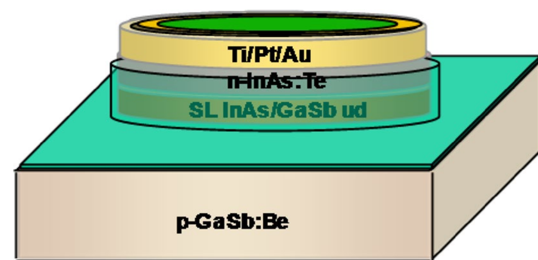

Fig. 1 The scheme of T2SL InAs/GaSb detector

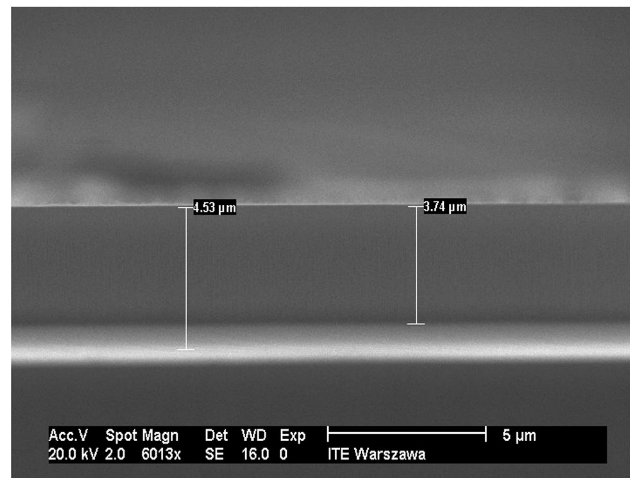

Fig. 2 The SEM image of the side wall of mesa structure in T2SL InAs/GaSb detector

The samples used in the experiments were the (100) oriented GaSb substrates doped with Te to the concentration of $n = 5{\times}10^{17}$ cm^{-3}. Prior to the chemical treatment in ODT and BPT solutions, the samples were cleaned in hot organic solvents (acetone and isopropanol), terminated by cold isopropanol rinse. The native oxides were reduced by etching of the GaSb surface for 1 min in 5% HCl followed by rinsing in degassed ethanol. The small amount of dissolved oxygen in ethanol was removed by bubbling with nitrogen for

30 min. Immediately after drying by nitrogen flow, the samples were immersed in a 10 mM ODT-C_2H_5OH or 10 mM BPT-C_2H_5OH solution at RT for 72 h, followed by rinsing in degassed ethanol and drying in nitrogen. The ODT was obtained from the Aldrich company in 98.9% purity while the BPT was received from Max Planck Institute for Polymer Research in Mainz [15, 16].

In the T2SL InAs/GaSb photodetector passivation experiments we used the 10 mM ODT-C_2H_5OH and for comparison the 21% $(NH_4)_2S$ solution. The SiO_2 dielectric layer with the thickness of 100 nm was deposited in the PVD 75 Kurt J. Lesker evaporation system.

The surface morphology was examined by atomic force microscopy (AFM) by means of the Bruker Innova AFM Microscope in the intermittent contact mode using Bruker probes, with the resonant frequency of $f_0 \approx 300$ kHz and the spring constant $k \approx 40$ N m^{-1}. The temperature ($T = 20$ °C) and humidity (50%) were maintained constant during the measurements performed in the air. The Nanotec WSxM software was used for the analysis of images [17]. All experiments were performed in the intermittent contact mode, where, except the height image, change of the cantilever oscillation phase (phase lag) is registered as well. This mode allows not only to significantly reduce the interaction between a probe and a sample but also brings additional information about the homogeneity of the scanned surface. The phase lag of an oscillating AFM cantilever depends on the mechanical properties of the scanned area such as hardness, elasticity or adhesion. Therefore, the phase image gives the opportunity to distinguish between the areas with different material properties. The optical microscope with submicron resolution is integrated with the AFM system.

The chemistry of a (100) GaSb surface was analyzed by Raman spectroscopy using Renishaw InVia Raman microscope equipped with a thermoelectrically (TE)-cooled CCD detector and an Ar^+ ion laser working at 514.5 nm wavelengths. The laser power at the focus spot (about 1 μm in diameter for ×50 objective, NA = 0.75) was kept below 0.5 mW. The position of the Raman peaks was calibrated before collecting the data using the Si sample as an external standard. The spectral resolution of the system was better than 2 cm^{-1}. The Raman spectra were measured in the 500–3200 cm^{-1} spectral range with the collection time ranging from 30 to 1200 s. The dynamics of ODT and BPT was simulated using the commercial program Gaussian 03 [18].

The calculations were carried out on an isolated molecule to determine the response of the molecular dynamics. The equilibrium geometry and vibration transitions of the investigated molecules were performed at B3LYP theory level using a basis set of 6-311++G(d,p). The B3LYP method is a hybrid density functional theory approach which combines the Becke's three-parameter nonlocal exchange potential with the Lee–Yang–Parr nonlocal correlation functional [19, 20]. The calculated frequencies were multiplied by the uniform factor of 0.98 to eliminate the systematic errors related to anharmonicity [21].

The scale factor used in the experiments is very close to that recommended for the B3LYP/6-311++G(d,p) calculations [22]. Since only the Raman scattering activities are obtained from Gaussian calculations, the theoretical Raman intensities were calculated using the procedure described in [23]. In the calculations, the temperature at which the data were collected ($T = 300$ K) and the excitation wavelength of the laser ($\lambda = 514.5$ nm) have been taken into account. The mode description was performed by the visual inspection of the individual modes using the GaussView program. The AFM and Raman spectroscopy measurements were preceded by the observations on the optical Olympus BX 51 microscope.

The contact angle of the (100) GaSb surface modified with ODT and BPT was measured by the manual deposition of the droplets (2 mm in diameter) of deionized water onto the GaSb surface using the Attension Theta Optical Tensiometer (KSV-NIMA Instruments). A water was purified by the Millipore Milli-Q purification system to the resistivity of $\rho = 18.2$ MΩ cm. The water droplet with a volume of 10 μl was gently deposited from a blunt-ended needle of a syringe after the syringe needle approached automatically the GaSb surface to the final distance of $d = 2$ mm. Each measurement was repeated two times at the temperature of $T = 20$ °C. The droplet images recorded by a CCD (charge-coupled device) camera have been analyzed with a droplet profile fitting method to determine the contact angle. All contact angles reported here are the average of 5 readings made on two independently prepared SAMs. The accuracy of measurements is ± 1°.

3 Results and discussion

3.1 Atomic force microscopy (AFM)

The AFM topography images on the (100) GaSb surface after the treatment in the 10 mM ODT-C_2H_5OH and the 10 mM BPT-C_2H_5OH are presented in Fig. 3a and b, respectively. The both surfaces are homogenous with a typical granular structure.

The grain size is not uniform with the lateral dimensions not exceeding 50 nm. It corresponds to maximally about 1.3×10^6 and 4.0×10^6 molecules constituting a grain of ODT and BPT, respectively. These values were estimated on the basis of the grain size and cross section of the ODT and BPT molecules, assuming that the cross-section is approximately a circle.

The AFM topography and phase images with the height profile on the (100) GaSb surface after the treatment in the

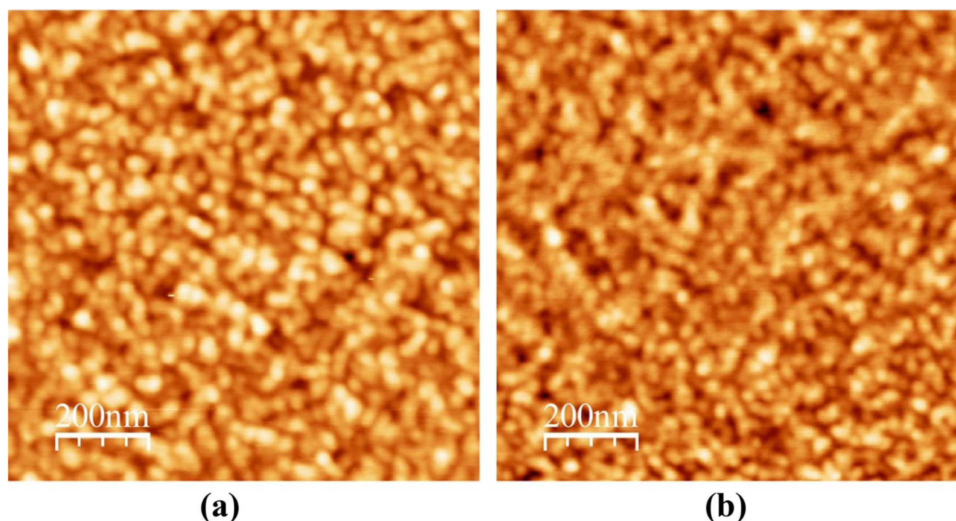

Fig. 3 AFM image of (100) GaSb surface after treatment in **a** 10 mM ODT-C_2H_5OH; **b** 10 mM BPT-C_2H_5OH (Scan size: 1 μm ×1 μm)

10 mM ODT-C_2H_5OH shown in Fig. 4 reveal the presence of 3-dimensional molecular forms visible as white regions with a diverse shape and an irregular borderline (Fig. 4a). We assume that the appearance of these molecular forms is the consequence of the investigated molecules aggregation. We note that the number of aggregates and their height are smaller for the BPT-covered GaSb surface (1 aggregate on the 20 μm^2 surface with a height of 3–20 nm) than for the ODT-covered GaSb surface (4 aggregates on the 20 μm^2

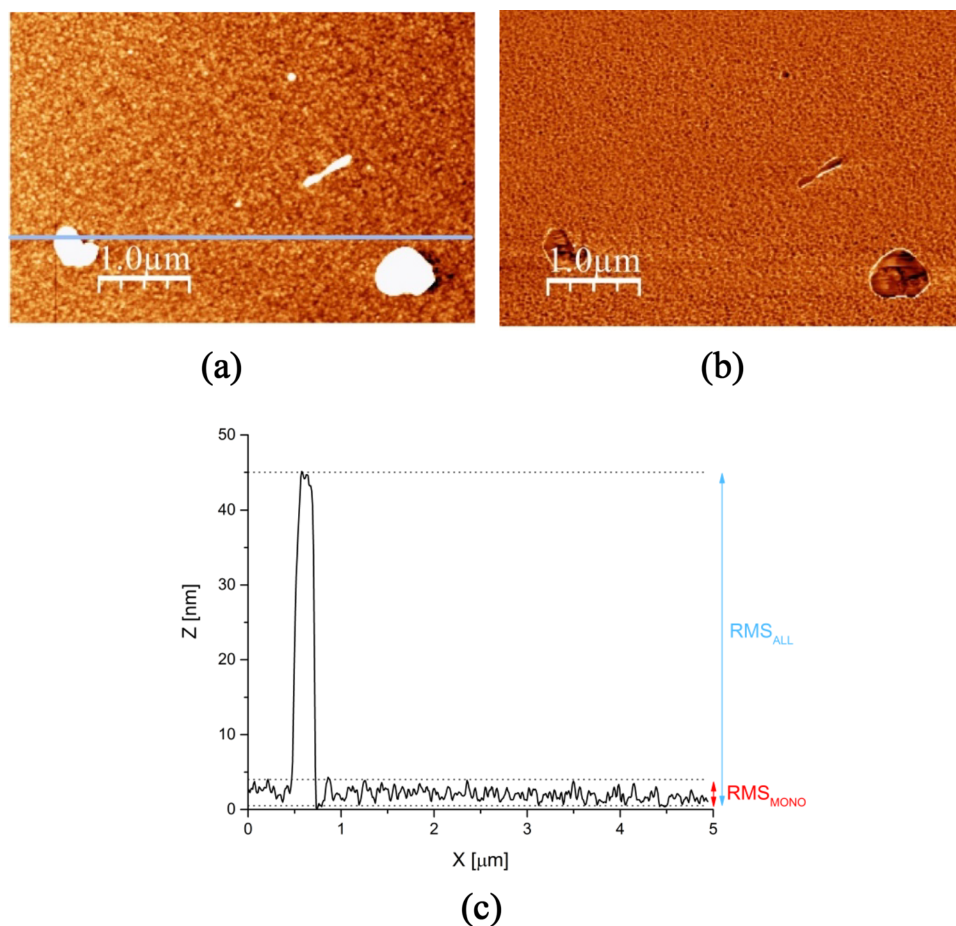

Fig. 4 (100) GaSb surface after treatment in 10 mM ODT-C_2H_5OH: **a** AFM image of surface topography; **b** the phase image; **c** the height profile (scan size: 5 μm ×3 μm)

surface with a height of 20–100 nm). It is consistent with the result of the optical microscope observations.

Figure 4a, b presents the topography and phase image of the same ODT-covered GaSb surface. This result allows to characterize the properties of the aggregates and their surroundings. While both areas are formed of the same ODT molecules, this informs that the difference between them derives only from the different molecular organization in a film and aggregate region. If both areas are formed of the same molecules, these images show the different molecular organization of aggregate regions and their surroundings. The topography and phase image of the BPT-covered GaSb surface are presented in Fig. 5. Table 1 contains the RMS (root means square) parameters for the ODT- and the BPT-covered GaSb surface. The RMS parameter was determined for the full range in the vertical scale (RMS_{ALL}) and for the range limited to the height excluding the aggregates (RMS_{MONO}), as shown in Fig. 4c. The bigger RMS_{ALL} for the ODT-covered GaSb surface is a consequence of the larger number of aggregates than for the BPT-covered surface. The RMS_{MONO} results from the roughness of the aggregates surroundings. The value of the RMS_{MONO} should be considered as the measure of the roughness of the film surrounding aggregates. For both the ODT- and the BPT-covered GaSb surface, this parameter is comparable to the thiol molecule dimensions. It suggests that thiol molecules adsorb onto the

Table 1 Roughness and Wenzel factor values for the ODT and the BPT films on (100) GaSb

GaSb surface coverage	RMS_{MONO} (nm)	RMS_{ALL} (nm)	R_W (a.u.)
ODT	0.79	5.97	1.005
BPT	0.77	0.89	1.003

surface in the Stranski–Krastanov growth model, a layer with islands growth [24].

The AFM results indicate that the ODT and the BPT layers can be homogenous in micrometric scale. They cover the GaSb surface almost perfectly without any cracks and holes. From the application point of view, another significant aspect is the wettability of the film. The factors determining wettability can have chemical or physical nature [25, 26]. The first one is determined by the terminal functional groups being in contact with the liquid. On the other hand, the physical effect originates from the altered contact area between solid and liquid in micro- and nanoscale due to the surface roughness. In extreme cases, the specific surface structure can significantly affect adhesion and lead to superhydrophobicity as in *lotus* or *petal effect*. Quantitatively, for the samples with a small RMS value, the impact of roughness on the observed contact angle is described by the Wenzel equation

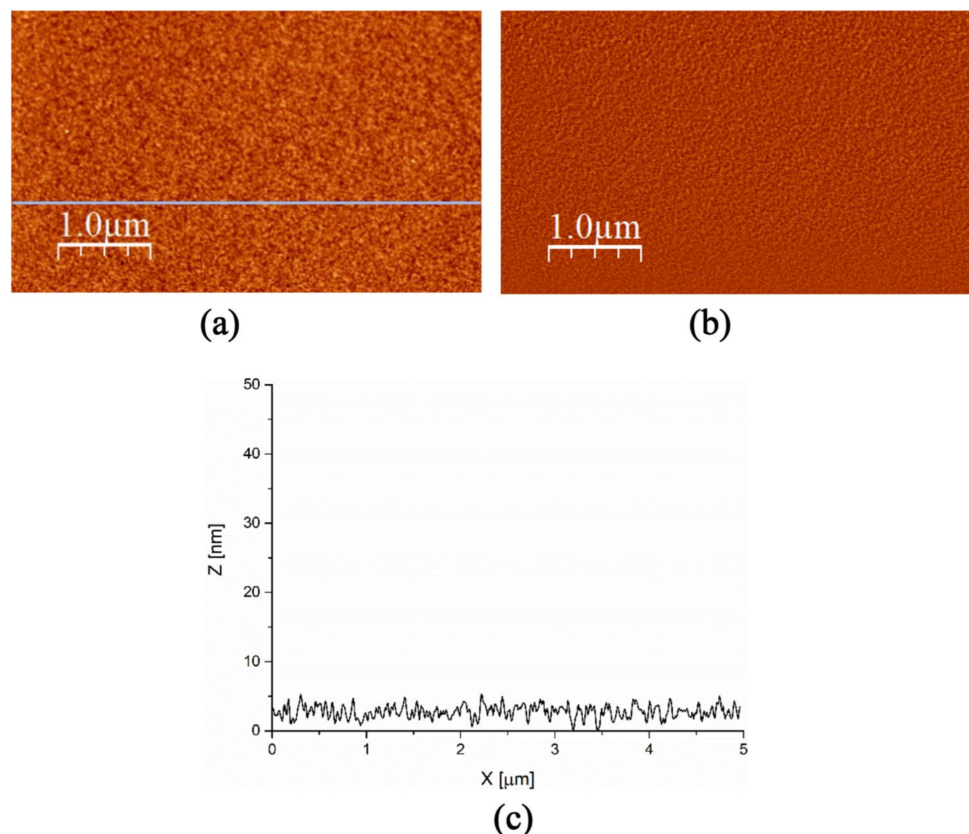

Fig. 5 (100) GaSb surface after treatment in 10 mM BPT-C_2H_5OH: **a** AFM image of surface topography; **b** the phase image; **c** the height profile (scan size: 5 µm ×3 µm)

$$\cos\theta_{APP} = R_W \cos\theta, \quad (1)$$

where θ_{APP} is observed contact angle, R_W is the Wenzel factor, and θ is the Young's contact angle.

The Wenzel factor was evaluated on the basis of AFM images according to the equation:

$$R_W = A_{APP}/A, \quad (2)$$

where A_{APP} is an apparent surface area and A is the geometric area.

The Wenzel factor R_W for both the ODT and the BPT was almost 1 (Table 1). We can conclude that the surface morphology does not affect the contact angle. The main reason of the difference in wettability probably results from the different structure of the ODT and the BPT molecules, in particular, the different terminal groups being in contact with water.

3.2 Raman spectroscopy

The results of the Raman spectroscopy measurements and theoretical calculations are presented in Figs. 6, 7 and Table 2. Figures 6a and 7a show the experimental spectra of the (100) GaSb surface passivated in the 10 mM ODT-C_2H_5OH and the 10 mM BPT-C_2H_5OH solutions, respectively, recorded at room temperature with the 514.5 nm excitation wavelength. It is worth noticing that in the presented spectral range only the Raman modes attributed to organic layers are observed. The DFT calculations were carried out to give the interpretation of the experimental results. Figures 6b and 7b show the results of the DFT calculations of the normal modes of the ODT and the BPT molecules. Table 2 contains the wavenumbers and corresponding to them assignments, resulting from both the experimental measurements of the thiols-passivated GaSb surface and the DFT calculations performed for the thiols molecules, and also the literature data necessary to interpret the results.

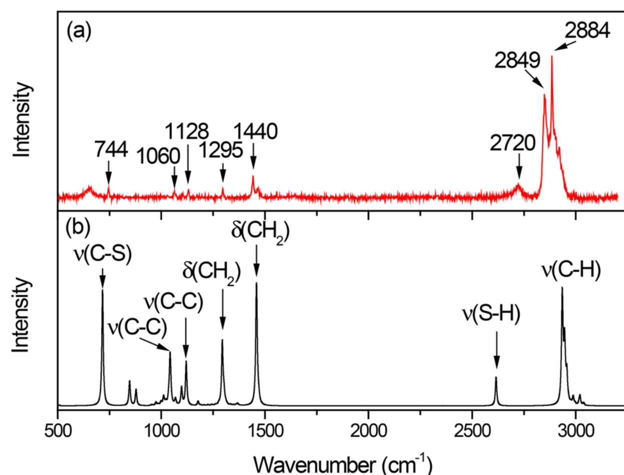

Fig. 6 **a** The Raman spectra of (100) GaSb passivated in 10 mM ODT-C_2H_5OH; **b** the calculated Raman spectra of the ODT molecule

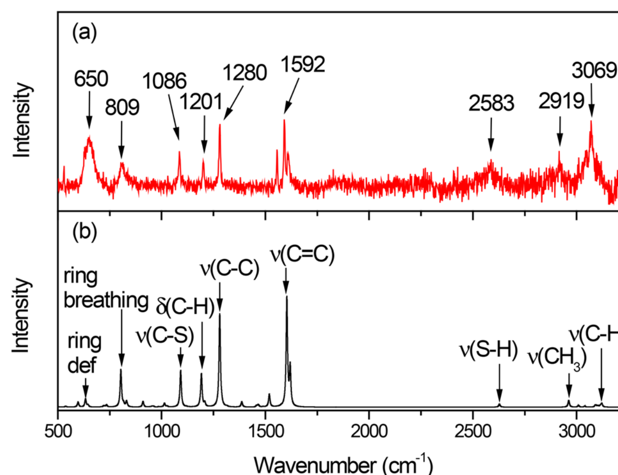

Fig. 7 **a** The Raman spectra of (100) GaSb passivated in 10 mM BPT-C_2H_5OH; **b** the calculated Raman spectra of the BPT molecule

As shown in Fig. 6a, in the spectral range below 1600 cm^{-1} one can find low-intensity modes at 744 cm^{-1} which can be assigned to the stretching vibrations of the C–S bonds [27–29], at 1060 cm^{-1} and 1128 cm^{-1} related to the stretching vibrations of the C–C bonds [27], and at 1295 cm^{-1} and 1440 cm^{-1} assigned to the twisting and scissoring vibrations of the CH_2 groups [27, 30]. In the spectral range from 2700 to 2950 cm^{-1} (Fig. 6a), the low-intensity mode at 2720 cm^{-1} and the group of bands between 2825 and 2950 cm^{-1} are visible. The mode at 2720 cm^{-1} is attributed to the stretching vibration of the S–H bonds [27, 29–31], seven modes at 2849, 2863, 2876, 2884, 2900, 2918, and 2933 cm^{-1} are assigned to the symmetric and antisymmetric stretching vibrations of the C–H bonds in CH_2 and CH_3 groups of the ODT molecule (Table 2) [27, 29, 31–35].

In the Raman spectrum of the surface passivated in the BPT solution, a few very low-intensity bands observed in the 600–1650 cm^{-1} spectral range (Fig. 7a) were attributed to the ring deformation at 650 cm^{-1}, the ring breathing vibrations at 809 cm^{-1}, the in-plane bending vibrations of the C–H bonds at 1201 cm^{-1}, the stretching vibrations of the C–C at 1280 cm^{-1}, and the C=C bonds of benzene ring at 1529 cm^{-1} [27, 29–31, 36].

Additionally, in the spectral range above 1650 cm^{-1}, a few very low-intensity modes are recorded. A band at 2583 cm^{-1} is assigned to the stretching vibration of the S–H bonds, while the bands in the range of 2900–3100 cm^{-1} are attributed to the stretching vibration of the C–H bonds [27, 32]. The comparative analysis of the results (Figs. 6, 7 and Table 2) indicates a good agreement between experimentally

Table 2 Wavenumbers and assignments of vibrational features of the ODT and the BPT layer on (100) GaSb surface

ODT layer				BPT layer			
Experimental	DFT calculation		Assignment	Experimental	DFT calculation		Assignment
$\tilde{\nu}$ (cm^{-1})	$\tilde{\nu}_{scal}$ (cm^{-1})	Raman scattering activity (Å^4/amu)		$\tilde{\nu}$ (cm^{-1})	$\tilde{\nu}_{scal}$ (cm^{-1})	Raman scattering activity (Å^4/amu)	
–	–	–	–	650	633	8.8312	ring def ip
744	716	28.7793	C–S str	–	–	–	–
–	–	–	–	809	804	70.4590	ring breathing
1060	1042	14.8175	C–C str	–	–	–	–
1100	1098	12.1711	C–C str	1086	1092	144.7361	C–S str
1128	1120	31.8590	C–C str	–	–	–	–
1172	1177	3.6742	C–C–C boop	1201	1192	162.1313	C–H b ip
1295	1294	65.2112	CH_2 tw	1280	1280	544.0225	C–C str
1440	1458	80.2102	CH_2 sc	–	–	–	–
1462	1469	7.9783	CH_3 b as	–	–	–	–
–	–	–	–	1592	1604	1146.0131	C=C str in benzene
–	–	–	–	1610	1620	419.3299	C=C str in benzene
–	–	–	–	2583	2628	144.7433	S–H str
2720	2616	224.7304	S–H str	–	–	–	–
2849	2934	470.1434	CH_2 str sym	–	–	–	–
2863	2935	662.2074	CH_2 str sym	–	–	–	–
2876	2945	336.5044	CH_2 str as	–	–	–	–
2884	2946	173.3418	CH_2 str as	–	–	–	–
2900	2957	192.8190	CH_3 str sym	–	–	–	–
2918	2986	15.5480	CH_2 str as	2919	2962	452.4007	CH_3 str sym
2933	3019	113.9064	CH_3 str as	–	–	–	–
–	–	–	–	3043	3115	112.6116	C–H str sym
–	–	–	–	3069	3122	272.0142	C–H str sym

Data multiplied by a scaling factor 0.98

def deformation, *str* stretching, *b* bending, *sym* symmetric, *as* antisymmetric, *ip* in plane, *oop* out of plane, *tw* twisting, *sc* scissoring

observed modes and theoretically calculated wavenumbers for the GaSb surface passivated in both the 10 mM ODT-C_2H_5OH and the 10 mM BPT-C_2H_5OH solution.

Raman spectroscopy studies indicate that there are no Raman active modes in the 600–3050 cm^{-1} spectral range for the bulk (100) GaSb surface Fig. 8). It is for this reason that the first- and the second-order Raman modes of GaSb surface show modes only below 500 cm^{-1} [37, 38].

Due to the presence of a greater amount of the islands with higher heights ranging from 20 to 100 nm (Fig. 3), the Raman spectrum of the GaSb surface passivated in the ODT solution has much higher intensity as compared to the spectrum recorded for the BPT-passivated surface. To obtain the Raman spectra of comparable intensity for both compounds, the collection time had to be increased from 180 s for the ODT-passivated surface to 1200 s for the BPT-passivated surface, whereas the other parameters were the same during the measurements. It is due to the greater scattering volume for the surface with greater aggregates. The measurements

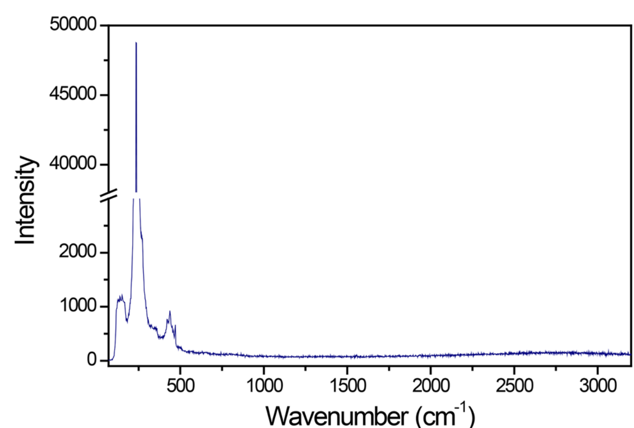

Fig. 8 The Raman spectrum of (100) GaSb surface recorded in 100–3200 cm^{-1} spectral range

outside the islands, carried out in the region of the grain-structured surface of both samples, do not allow to register the Raman spectra of thiols layers. It is because the spontaneous Raman scattering technique has too small sensitivity to register the Raman spectrum from the very thin ODT and BPT layers, since the amount of scattering material is too small to register the spectrum.

3.3 Contact angle measurement

The contact angle of the deposited droplets of water onto the (100) GaSb surface before and after passivation in the 10 mM ODT-C_2H_5OH or the 10 mM BPT-C_2H_5OH reveals the macroscopic changes of the surface-free energy, contrary to the information about the ODT and the BPT adsorption received from the AFM images in nanometric scale. The results of the measurements of the surface wetting by pure water performed 5 days after the thiols passivation are presented in Table 3 and Fig. 9. The values of the static contact angle obtained immediately after the water droplet deposition ($t = 10$ s after the surface wetting) and $t = 30$ s later, as well as automatically calculated droplet volumes are summarized in Table 3. The information about the droplet size is important for assessing the impact of distortion drops by gravitation. The shape of a sufficiently small droplet is not distorted by gravitation and the contact angle depends only on surface tensions. The minimal change of volume after 30 s (from 9.9 to 9.8 µl for the GaSb surface) indicates that the drop does not dry up.

Figure 9 shows the recorded droplet images obtained for the (100) GaSb surface: (a) without passivation, (b) after passivation by the 10 mM ODT-C_2H_5OH solution, and (c) after passivation by the 10 mM BPT-C_2H_5OH. The static contact angle was changed both after the ODT and BPT passivation, amounted to 78° and 68°, respectively.

These results indicate that the GaSb surface has been modified and they are consistent with the data received from the AFM studies, although the AFM images provide information on a nanoscale, while the contact angle measurements concern the surface at the macro-scale. The AFM images (Figs. 3, 4 and 5) show evidently the presence of the SAMs on the GaSb surface. The difference between the received values for ODT and BPT-passivated surfaces indicates the changes of the surface-free energy or/and topography. The lower contact angle value of the BPT monolayer compared to ODT is connected with specific electronic properties of two phenyl rings of BPT molecules making the monolayer more hydrophilc. The monolayer of BPT adsorbed on the GaSb surface is much better oriented and densely packed thanks to the attraction of the biphenyl rings of neighboring molecules than the ODT layer. The received values of contact angles are consistent with the literature data for the (100) GaAs surface modified with alkanethiols, especially for the short carbon chains [39]. Additionally, the changes of the contact angle of the GaSb surface passivated by the thioles, stored under ambient conditions, were also investigated. The decrease in the contact angle after 1 month was ~ 1°

Table 3 Contact angle of (100) GaSb surface passivated by ODT and BPT

Surface	Contact angle (°)		Volume of drop (µl)	
	α_{10} (after 10 s)	α_{30} (after 30 s)	V_{10} (after 10 s)	V_{30} (after 30 s)
(100) GaSb	83	82	9.9	9.8
(100) GaSb passivated by ODT	78	77	9.9	9.8
(100) GaSb passivated by ODT after 1 month	77	77	10.0	9.8
(100) GaSb passivated by BPT	68	68	9.8	9.7
(100) GaSb passivated by BPT after 1 month	54	52	9.4	9.3

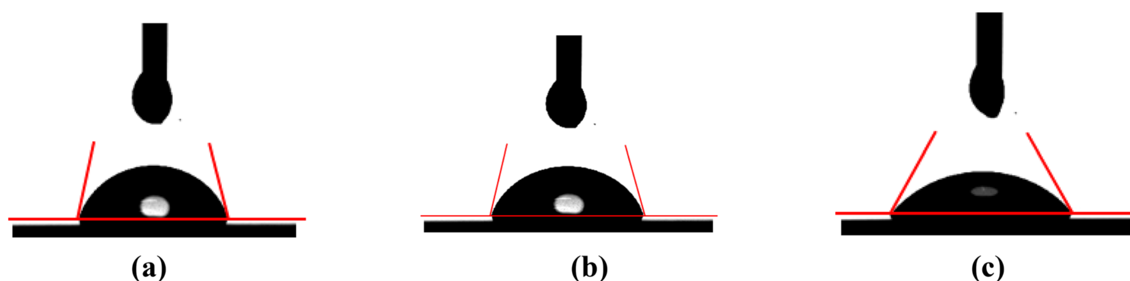

Fig. 9 Schematic presentation of contact angle of a water droplet onto (100) GaSb surface **a** before passivation; **b** after passivation in 10 mM ODT-C_2H_5OH; **c** after passivation in 10 mM BPT-C_2H_5OH

for ODT and ~ 15° for BPT monolayers, indicating that the thioles are still present on the GaSb surface; however, the ODT SAMs are more stable than BPT.

3.4 Current–voltage characteristic

The passivation effectiveness has been controlled by current–voltage characteristics. The electrical characteristics at 225 K, obtained for the T2SL InAs/GaSb photodetector, before and after passivation using three different methods, are presented in Fig. 10. It includes the $(NH_4)_2S$ passivation, the SiO_2 coating after the ODT passivation in the 10 mM ODT-C_2H_5OH (ODT + SiO_2) and the SiO_2 coating only. The results of the contact angle analysis showed the higher term stability for ODT SAMs compared to BPT SAMs (Table 3); therefore, the ODT SAMs were chosen for the two-step passivation (ODT + SiO_2). Generally, the application of passivation caused the reduction of a dark current regardless of the chosen method as compared to the unpassivated devices. The largest decrease of about an order of magnitude was observed for the detector with the two-step passivation consisting of the ODT and the SiO_2 coating. Probably, the ODT played the main role of an electrical passivant, whereas the SiO_2 layer provides protection against environmental exposure. The increase in the dark current density at high reverse bias for the SiO_2-passivated surface was caused by the variation in a doping concentration profile. It is necessary to further study the two-step passivation, in particular, the role of the ODT and the SiO_2 as the passivants.

In Fig. 11, dark current density as a function of reciprocal temperature at 50 mV reverse bias is shown for unpassivated and ODT + SiO_2 passivated photodetectors. The choice of devices to compare was dictated the highest decrease in the dark current among all aforementioned types of passivation.

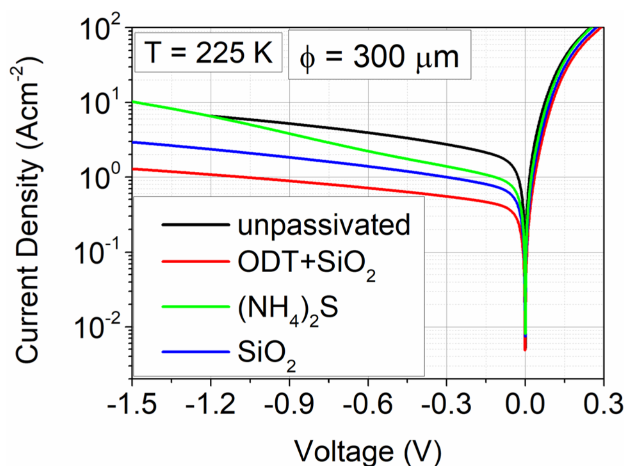

Fig. 10 Current-voltage characteristics at 225 K for T2SL InAs/GaSb photodetectors: unpassivated and passivated by two-step treatment (ODT + SiO_2), in 21% $(NH_4)_2S$ and SiO_2

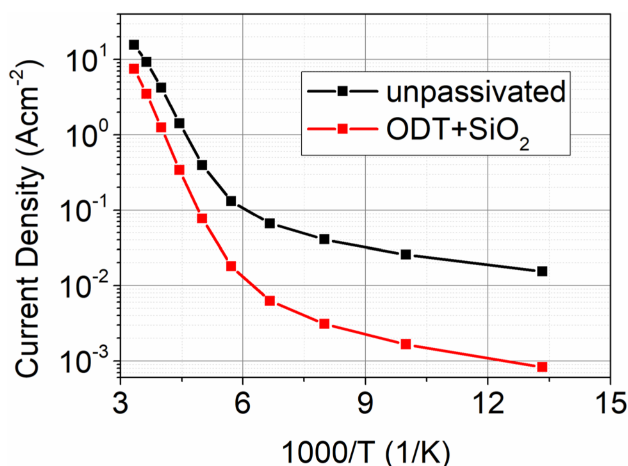

Fig. 11 Current density versus reciprocal temperature for unpassivated and ODT + SiO_2 passivated photodetectors at 50 mV reverse bias

The measurements were performed in the temperature range from 75 K to 300 K. Passivated device was characterized by smaller dark current density than the unpassivated one in the entire temperature range. The difference increased with decreasing temperature.

Besides electrical characterization of the detectors a spectral current responsivity measurement were performed to check for any negative impact of passivation on the optical performance. In Fig. 12, a comparison between responsivity of unpassivated and ODT + SiO_2-passivated devices at zero bias and at 225 K is presented. The responsivities for both samples are very close to each other and any variations are small enough that the dark current has far more influence on the overall performance (noise and detectivity). A small difference in the cutoff wavelength between the detectors was observed. It can be explained by the nonuniformity of the epitaxial material on the substrate, which is a result of

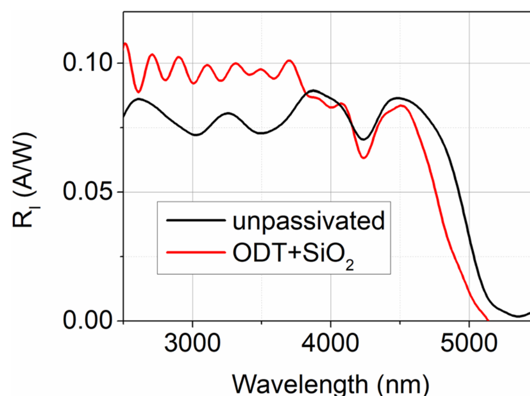

Fig. 12 Spectral current responsivity for unpassivated and ODT + SiO_2-passivated photodetectors measured at zero bias and at 225 K

MBE reactor configuration that was used for the growth of detector heterostructures.

4 Conclusions

In conclusion, the new two-step passivation with SiO_2 coating after the 10 mM ODT-C_2H_5OH wet treatment was used for T2SL InAs/GaSb infrared detector. To understand the mechanism of passivation, the (100) GaSb surface covered with the ODT and, for comparison, the BPT SAMs was characterized by the AFM, Raman spectroscopy and contact angle measurement. The AFM images show the homogeneous surface with the typical granular structure for both ODT and BPT monlayers; however, the presence of the aggregates was also observed. The results of Raman spectroscopy strengthened by DFT calculations confirm the presence of the ODT and BPT layers on (100) GaSb surface. The change of contact angle after both the 10 mM ODT-C_2H_5OH and the 10 mM BPT-C_2H_5OH wet treatment indicated the evidence presence of ODT and BPT monolayers, respectively. In addition, the decrease in the contact angle after 1 month was ~ 1° for ODT and ~ 15° for PBT, indicating that the thioles are still present on the GaSb surface; however, the ODT SAMs are more stable than BPT.

Consequently, using the two-step passivation by ODT-based wet treatment and following SiO_2 layer deposition allowed to improve the performance of T2SL InAs/GaSb detector. The dark current was reduced by one order of magnitude for passivated detector, where the second step—the SiO_2 coating—can act as encapsulation.

Acknowledgements This work was partially supported by the Research Project of the Polish Ministry of Science and Higher Education 06/65/SBAD/1952 and The National Centre for Research and Development, Poland under project No.TECHMATSTRATEG1/347751/5/NCBR/2017. The authors are grateful to Prof. Hans Jörgen Butt (Max Planck Institute for Polymer Research in Mainz) for providing the biphenyl thiol BPT for the experiments and Dr Jacek Ratajczak (Łukasiewicz Research Network - Institute of Electron Technology in Warsaw) for the SEM image.

Open Access This article is distributed under the terms of the Creative Commons Attribution 4.0 International License (http://creativecommons.org/licenses/by/4.0/), which permits unrestricted use, distribution, and reproduction in any medium, provided you give appropriate credit to the original author(s) and the source, provide a link to the Creative Commons license, and indicate if changes were made.

References

1. C.L. Tan, H. Mohseni, Nanophotonics **7**(1), 169 (2018)
2. S. Wang, N. Yoon, A. Kamboj, P. Petluru, W. Zheng, D. Wasserman, Appl. Phys. Lett. **112**, 091104 (2018)
3. A. Karim, R. Marcks von Würtemberg, C. Asplund, H. Malm, J. Andersson, E. Plis, S. Krishna, Phys. Status Solidi C **9**(7), 1690 (2012)
4. A. Hood, P.-Y. Delaunay, D. Hoffman, B. Nguyen, Y. Wei, M. Razeghi, Appl. Phys. Lett. **90**, 233513 (2007)
5. H.S. Kim, E. Plis, N. Guatam, S. Myers, Y. Sharma, L.R. Dawson, Appl. Phys. Lett. **97**, 143512 (2010)
6. A. Gin, Y. Wei, A. Hood, A. Bajowala, V. Yazdanpanah, M. Razeghi, M. Tidrow, Appl. Phys. Lett. **84**, 2037 (2004)
7. R. Rehm, M. Walter, F. Fuchs, J. Schmitz, J. Fleissner, Appl. Phys. Lett. **86**, 173501 (2005)
8. E. Papis-Polakowska, J. Kaniewski, J. Szade, W. Rzodkiewicz, A. Jasik, J. Jurenczyk, A. Wawro, Thin Solid Films **567**, 77 (2014)
9. E. Papis-Polakowska, J. Kaniewski, J. Jurenczyk, A. Jasik, K. Czuba, A.E. Walkiewicz, J. Szade, AIP Advanced **6**, 0552061 (2016)
10. G.M. Marshall, G.P. Lopinski, F. Bensebaa, J.J. Dubowski, Nanotechnology **22**, 235704 (2011)
11. D. Cuypers, C. Fleischmann, D.H. Dorp, S. Brizzi, M. Tallarida, M. Müller, P. Hönicke, A. Billen, R. Chintala, T. Conard, D. Schmeißer, W. Vandervorst, S. Van Elshocht, S. Armini, S. De Gendt, C. Adelmann, Chem. Mater. **28**(16), 5689 (2016)
12. M. Schvartzman, V. Sidorov, D. Ritter, Y. Paz, J. Vac. Sci. Technol. B **21**, 148 (2003)
13. H.A. Budz, M.C. Biesinger, R.R. LaPierre, J. Vac. Sci. Technol. B **27**(2), 637 (2009)
14. P. Arudra, G.M. Marshall, N. Liu, J.J. Dubowski, J. Phys. Chem. C **116**, 2891 (2012)
15. H. Gojzewski, M. Kappl, H.J. Butt, A. Ptak, Langmuir **32**, 4500 (2016)
16. H. Gojzewski, M. Kappl, G. Kircher, W. Koczorowski, H.J. Butt, A. Ptak, Chem. Phys. Chem. **14**, 543 (2013)
17. I. Horcas, R. Fernandez, J.M. Gomez-Rodriguez, J. Colchero, J. Gomez-Herrero, A.M. Baro, Rev. Sci. Instrum. **78**(1), 013705 (2007)
18. M.J. Frisch, G.W. Trucks, H.B. Schlegel, G.E. Scuseria, M.A. Robb, J.R. Cheeseman, J.A.Montgomery, J.T. Vreven, K.N. Kudin, J.C. Burant, J.M. Millam, S.S. Iyengar, J. Tomasi, V. Barone, B. Mennucci, M. Cossi, G. Scalmani, N. Rega, G.A. Petersson, H. Nakatsuji, M. Hada, M. Ehara, K. Toyota, R. Fukuda, J. Hasegawa, M. Ishida, T. Nakajima, Y. Hona, O. Kitao, H. Nakai, M. Klene, X. Li, J.E. Knox, H.P. Hratchian, J.B. Cross, C. Adamo, J. Jaramillo, R. Gomperts, R.E. Stratmann, O. Yazyev, A.J. Austin, R. Cammi, C. Pomelli, J.W. Ochterski, P.Y. Ayala, K. Morokuma, G.A. Voth, P. Salvador, J.J. Dannenberg, V.G. Zakrzewski, S. A. Dapprich, D. Daniels, M.C. Strain, O. Farkas, D.K. Malick, A.D. Rabuck, K. Raghavachari, J.B. Foresman, J.V. Ortiz, Q. Cui, A.G. Baboul, S. Clifford, J. Cioslowski, B.B. Stefanov, G. Liu, A. Liashenko, P. Piskorz, I. Komaromi, R.L. Martin, D.J. Fox, T. Keith, M.A. Al-Laham, C.Y. Peng, A. Nanayakkara, P.M.W. Challacombe Gill, B. Johnson, W. Chen, M.W. Wong, C. Gonzalez, J.A. Pople, Gaussian 03 (Revision B.03) (Gaussian, Inc., Pittsburgh, 2003)
19. A.D. Becke, J. Chem. Phys. **98**, 5648 (1993)
20. M.J. Frisch, J.A. Pople, J.S. Binkley, J. Chem. Phys. **80**, 3265 (1984)
21. J.P. Merrick, D. Moran, L. Radom, J. Phys. Chem. A **111**, 11683 (2007)
22. A.P. Scott, L. Radom, J. Phys. Chem. **100**, 16502 (1996)
23. R. Sun, J. Yao, S. Li, R. Gu, Vib. Spectrosc. **47**, 38 (2008)
24. D.G. de Oteyza, E. Barrena, Y. Zhang, T.N. Krauss, A. Turak, A. Vorbiev, H. Dosch, J. Phys. Chem. C **113**(11), 4234 (2009)
25. J.N. Israelachvili, *Intermolecular and Surface Forces*, 3rd edn. (Academic Press, Elsevier, 2011)

26. H.J. Butt, K. Graf, M. Kappl, *Physics and Chemistry of Interfaces* (Wiley-VCH GmbH & KGaA, Weinhei, 2003)
27. M.A. Bryant, J.E. Pemberton, J. Am. Chem. Soc. **113**, 3629 (1991)
28. A. Kudelski, Vib. Spectrosc. **39**, 200 (2005)
29. A. Kudelski, Langmuir **19**, 3805 (2003)
30. A. Pallipurath, O. Nicoletti, J.M. Skeleton, S. Mahajan, P.A. Midgley, S.R. Elliott, Ultrason. Sonochem. **21**, 1886 (2014)
31. C.S. Levin, B.G. Janesko, R. Bardhan, G.E. Scuseria, J.D. Hartgerink, N.J. Halas, Nano Lett. **6**, 2617 (2006)
32. C.W. Meuse, G. Niaura, M.L. Lewis, A.L. Plant, Langmuir **14**, 1604 (1998)
33. W. Knoben, S.H. Brougersma, M. Crego-Calma, J. Phys. Chem. C **113**, 18331 (2009)
34. C. Vericat, M.E. Vela, G. Corthey, E. Peusa, E. Cortes, M.H. Fonticelli, F. Ibanez, G.E. Benitez, P. Carro, R.C. Salvarezza, RSC Adv. **4**, 27730 (2014)
35. O.S. Nakagawa, S. Ashok, C.W. Sheen, J. Martensson, D.L. Allara, Jpn. J. Appl. Phys. **30**, 3759 (1991)
36. P.Z. El-Khoury, D. Hu, V.A. Apkarian, W.P. Hess, Nano Lett. **13**, 1858 (2013)
37. P.B. Klein, R.K. Chang, Phys. Rev. B. **14**, 2498 (1976)
38. H. Liu, N. Yue, Y. Zhang, P. Qiao, D. Zuo, B. Kesler, S.L. Chuang, J.H. Ruou, J.D. Justice, R. Dupuis, Phys. Rev. B. **91**, 235317 (2015)
39. S. Ye, G. Li, H. Noda, K. Uosaki, M. Osawa, Surf. Sci. **529**, 163 (2003)

Publisher's Note Springer Nature remains neutral with regard to jurisdictional claims in published maps and institutional affiliations.